AD-A185 483 TENSILE STRENGTH OF FROZEN SILT(U) COLD REGIONS RESEARCH AND ENGINEERING LAB HANOVER NH Z YUANLIN ET AL. AUG 87 CRREL-87-15 1/1

UNCLASSIFIED F/G 8/10 NL

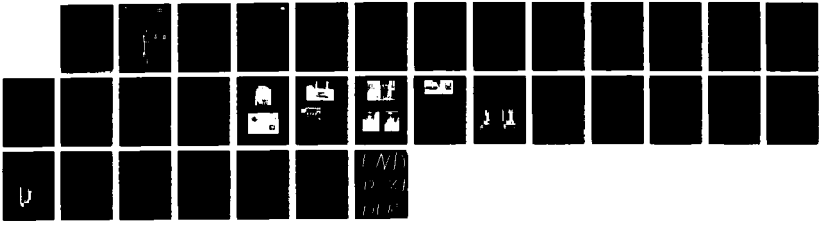

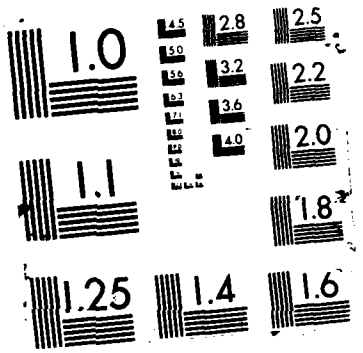
1.0
1.1
1.25
1.4
1.6
2.8
3.2
3.6
4.0
2.5
2.2
2.0
1.8

CRREL REPORT 87-15

US Army Corps of Engineers
Cold Regions Research & Engineering Laboratory

AD-A185 483

Tensile strength of frozen silt

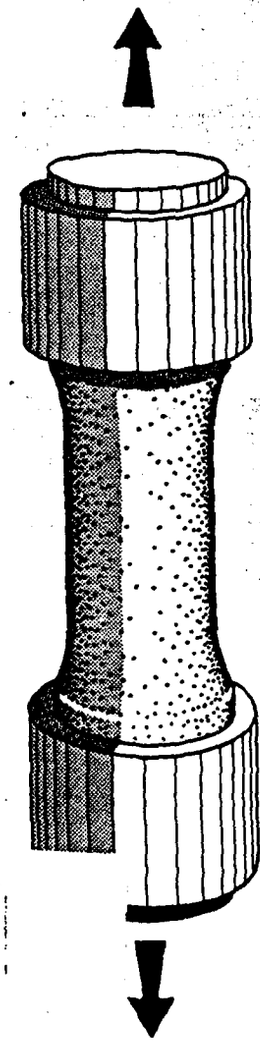

For conversion of SI metric units to U.S./British customary units of measurement consult ASTM Standard E380, Metric Practice Guide, *published by the American Society for Testing and Materials, 1916 Race St., Philadelphia, Pa. 19103.*

CRREL Report 87-15

August 1987

Tensile strength of frozen silt

Zhu Yuanlin and David L. Carbee

UNCLASSIFIED
SECURITY CLASSIFICATION OF THIS PAGE

A185 483

REPORT DOCUMENTATION PAGE

Form Approved
OMB No 0704-0188
Exp. Date Jun 30, 1986

1a. REPORT SECURITY CLASSIFICATION Unclassified	1b. RESTRICTIVE MARKINGS
2a. SECURITY CLASSIFICATION AUTHORITY	3. DISTRIBUTION/AVAILABILITY OF REPORT Approved for public release; distribution is unlimited.
2b. DECLASSIFICATION/DOWNGRADING SCHEDULE	
4. PERFORMING ORGANIZATION REPORT NUMBER(S) CRREL Report 87-15	5. MONITORING ORGANIZATION REPORT NUMBER(S)
6a. NAME OF PERFORMING ORGANIZATION U.S. Army Cold Regions Research and Engineering Laboratory 6b. OFFICE SYMBOL (If applicable) CRREL	7a. NAME OF MONITORING ORGANIZATION
6c. ADDRESS (City, State, and ZIP Code) 72 Lyme Road Hanover, New Hampshire 03755-1290	7b. ADDRESS (City, State, and ZIP Code)
8a. NAME OF FUNDING/SPONSORING ORGANIZATION 8b. OFFICE SYMBOL (If applicable)	9. PROCUREMENT INSTRUMENT IDENTIFICATION NUMBER ILIR No. 4A161101A91D
8c. ADDRESS (City, State, and ZIP Code)	10. SOURCE OF FUNDING NUMBERS PROGRAM ELEMENT NO. / PROJECT NO / TASK NO. / WORK UNIT ACCESSION NO

11. TITLE (Include Security Classification)

Tensile Strength of Frozen Silt

12. PERSONAL AUTHOR(S)
Zhu Yuanlin and David L. Carbee

13a. TYPE OF REPORT	13b. TIME COVERED	14. DATE OF REPORT (Year, Month, Day)	15. PAGE COUNT
	FROM _____ TO _____	August 1987	29

16. SUPPLEMENTARY NOTATION

17. COSATI CODES			18. SUBJECT TERMS (Continue on reverse if necessary and identify by block number)	
FIELD	GROUP	SUB-GROUP		
			Frozen mechanics	Soil
			Frozen soil	Strain
			Silt	Strength

19. ABSTRACT (Continue on reverse if necessary and identify by block number)

Constant strain-rate tension tests were conducted on remolded saturated frozen Fairbanks silt at various temperatures, strain rates, and densities. It was found that the critical strain rate of the ductile-brittle transition is not temperature-dependent at temperatures down to -5°C, but varies with density. The transition occurs at a strain rate of 10^{-2}/s for medium-density silt and 5×10^{-4}/s for low-density silt. The peak tensile strength decreases considerably with decreasing strain rate for ductile failure, but it decreases slightly with increasing strain rate for brittle fracture. The failure strain remains almost constant at temperatures lower than about -2°C, but it varies with density and strain rate at -5°C. The initial tangent modulus is independent of strain rate and increases with decreasing temperature and density.

20. DISTRIBUTION/AVAILABILITY OF ABSTRACT	21. ABSTRACT SECURITY CLASSIFICATION	
☒ UNCLASSIFIED/UNLIMITED ☐ SAME AS RPT ☐ DTIC USERS	Unclassified	
22a. NAME OF RESPONSIBLE INDIVIDUAL DAVID CARBEE	22b. TELEPHONE (Include Area Code) 603-646-4477	22c. OFFICE SYMBOL CECRL-EG

DD FORM 1473, 84 MAR 83 APR edition may be used until exhausted
All other editions are obsolete

SECURITY CLASSIFICATION OF THIS PAGE
UNCLASSIFIED

PREFACE

This report was prepared by Zhu Yuanlin, visiting associate professor on leave from the Lanzhou Institute of Glaciology and Geocryology, Academia Sinica, China, and David L. Carbee, Research Technician, Geotechnical Research Branch, Experimental Engineering Division, U.S. Army Cold Regions Research and Engineering Laboratory.

This study was funded through an FY83/84 ILIR (In-house Laboratory Independent Research) program, No. 4A161101A91D, *Mechanical Properties of Frozen Silt,* which includes three basic subjects: uniaxial compression, tension, and triaxial compression laboratory studies. This report covers the results of the tension tests on frozen Fairbanks silt.

The authors acknowledge W. Quinn, E. Chamberlain, F. Sayles, D. Cole, J. Bayer, and G. Durell for their technical advice and instrumentation assistance. Thanks are also due to Dr. M. Mellor and Dr. F.D. Haynes for helpful discussions, and especially to F. Sayles and D. Cole for their very careful and fruitful review of this final report.

CONTENTS

ILLUSTRATIONS

NOMENCLATURE

a	temperature-dependent parameter (kg/cm^2)
A	empirical parameter (kg/cm^2)
A_0	initial cross-sectional area of specimen
b	temperature-dependent parameter
B	time parameter (s)
e	void ratio of soil specimen
E_i	initial tangent modulus (kg/cm^2)
E_1	50% peak strength modulus (kg/cm^2)
G	specific gravity of soil
G_i	specific gravity of ice
i_v	volume ice content
k	stress parameter (kg/cm^2)
m	empirical parameter
n	dimensionless parameter
N	number of data points
S	degree of saturation
t_m	time to failure (s)
v	machine speed (cm/min)
w	water content (%)
w_u	unfrozen water content (%)
β	stress parameter (kg/cm^2)
ΔL	corrected deformation in neck of specimen
ΔL_t	observed deformation of entire specimen
γ	correlation coefficient
γ_d	dry density (g/cm^3)
ϵ_f	failure strain
$\dot{\epsilon}$	average strain rate (per second)
$\dot{\epsilon}_1$	reference strain rate (1.0/s)
σ	true stress (kg/cm^2)
σ_m	peak tensile strength (kg/cm^2)
σ_0	limiting instantaneous strength
θ	temperature (°C)
θ_0	reference temperature (-1.0°C)

Tensile Strength of Frozen Silt

ZHU YUANLIN AND DAVID L. CARBEE

INTRODUCTION

The design of structures in cold regions sometimes requires information on the tensile strength of frozen soils. Unfortunately, very few studies have been done on this subject to date. Haynes et al. (1975) investigated the effect of strain rate on the tensile strength of frozen Fairbanks silt with high density at -9.4°C. A ductile-brittle transition was reported, occurring at a strain rate of about 10^{-2}/s.

The purpose of this study is to investigate the effect of temperature, strain rate, and density on the tensile strength of remolded saturated frozen Fairbanks silt. The test program was as follows: 1) the samples with medium density were tested under various machine speeds from 5.9×10^{-5} to 5.9×10^{2} cm/min at -2 and -5°C; 2) the medium density specimens were also tested at various temperatures from -1 to -10°C under a machine speed of 5.9×10^{-2} cm/min; and 3) the specimens with three different densities were tested at the machine speed of 5.9×10^{-2} cm/min and a temperature of -5°C. The three desired densities are 1.4 (high), 1.2 (medium), and 1.1 g/cm^3 (low), respectively.

TESTING

Material

The material used in this study was a remolded silt taken from the USACRREL experimental permafrost tunnel at Fox, near Fairbanks, Alaska. The silt is classified as ML in the plasticity chart with approximately 94% passing the #200 mesh sieve and 17% finer than 0.01 mm. Its main physical properties are as follows:

Plastic limit	34.2%
Liquid limit	38.4%
Organic content	5.49%
Specific gravity	2.680

Specimen preparation

Molding

Distilled water was added to the air-dried Fairbanks silt, making a silt-water mixture with an initial molding water content of 12% by weight. After being stored one day to allow moisture equilibration, the moist silt was then carefully compacted to the desired density in a cast acrylic gang mold in six layers as shown in Figure 1. The mold, described in detail by Haynes (1975), can form four 25.4-mm-diameter by 82.55-mm-long dumbbell specimens at a time.

Saturating

After compaction, the samples were saturated with de-aerated, distilled water under a vacuum of 73 mm Hg. The saturation system is shown in Figure 2.

Freezing

When the samples were saturated, they were placed in a freezing cabinet and quickly frozen from the top down in an open system at -30°C. Figure 3 shows the freezing cabinet with a specimen-charged mold ready to be set up for freezing. To obtain rapid frost penetration and thus minimize ice lensing during freezing, the specimens were allowed to equilibrate at 0°C in the cabinet overnight before freezing. Some minor ice lenses parallel to the frost penetration are still visible in the specimens with low density, even though the freezing process is carefully controlled. After freezing, the mold was taken from the cabinet and carefully disassembled in a coldroom, as shown in Figure 4.

Dimension of specimen

One-half of the specimen geometry is illustrated in Figure 5. The neck-down portion of the dumbbell-shaped specimen is 50.8 mm long and 25.4 mm in diameter.

Testing procedure and apparatus

The tension tests were conducted on a Model 16000 MTS closed-loop electrohydraulic testing machine operated in "stroke" control. This mode of control is equivalent to a constant cross-head speed test. A Ransco refrigeration unit with a dual-chambered temperature-controlled cabinet was installed in conjunction with the MTS machine. The two chambers (an air-temperature conditioning and a test chamber) are connected through large insulated air transfer hoses. Figure 6 shows the MTS machine and the installed testing cabinet. Before testing, each specimen was tempered in the cabinet at the test temperature for at least 24 hours. The environmental temperature around the specimen was measured by a digital thermometer with a sensitivity of 0.01°C. Observation has shown that its fluctuation is less than ±0.05°C during tests.

The axial tensile load was measured by a multi-range load cell accessory to the MTS machine, Model 661.21A-03. The elongation of the neck section of a specimen was measured by two extensometers, which were held to the surface of the specimen by rubber bands, as shown in Figure 7. The gauge length of the extensometers is 50.8 mm with a 10.2 mm range. Two edges of each extensometer were carefully set up on the surface at both ends of the neck section of a specimen. The average values of the elongation measured by the two extensometers were then used to calculate the strain of the specimen. For some of the tests, the elongation of the specimens between the two end caps was also measured by two LVDTs (linear variable differential transformers), Model 200-DCD, which were mounted on the end caps, as shown in Figure 8.

To protect specimens from sublimation during testing, the surface of specimens tested at machine speeds less than 5.9×10^{-3} cm/min was coated with a thin layer of silicone grease.

During a test, the tensile load and the elongation of the specimen were recorded by a strip-chart recorder and a Kaye Model 8400 data logger (for slow tests) or a Biomation Model 1015 transient recorder together with a Type 203 oscilloscope (for fast tests). These two instruments are shown in Figure 9. The environmental temperature was recorded by a strip-chart recorder.

After testing, the neck section of each specimen was removed for water content and density measurement.

RESULTS

The results of the constant strain-rate tension test are summarized in Tables 1, 2, and 3. The peak (or ultimate) strength σ_m refers to the maximum stresses on the true stress vs true strain* curves. Correspondingly, the failure strain ϵ_f and the time to failure t_m refer to the strain and time at the peak strength, respectively. The initial tangent modulus E_i and the 50% strength modulus E_1 are determined graphically. The average strain rate is computed by $\dot{\epsilon} = \epsilon_f/t_m$. If there was no data for ϵ_f and t_m, the average strain rate was then taken as a nominal value corresponding to the applied machine speed.

The physical properties of the specimens are shown in Appendix A. Note that water content w and dry density γ_d are taken from the specimens after testing. The volume ice content i_v is calculated by

$$i_v = \frac{(w - w_u)\gamma_d}{G_i \gamma_w} \tag{1}$$

where G_i is the specific gravity of ice taken as 0.917, γ_w is the unit weight of water taken as 1 g/cm³, and w_u is the unfrozen water content of the specimens. The values of w_u of Fairbanks silt with various total water contents are shown in Appendix B. The saturation degree S is computed by

$$S = \frac{100[w - (1 - G_i)w_u]G}{G_i e} \ (\%) \tag{2}$$

where G is the specific gravity of the soil particles, equal to 2.68 for the soil tested, and e is the void ratio of the specimens.

DISCUSSION

Stress-strain curves and failure mode

Figure 10 presents a set of typical stress-strain curves of the samples with medium density for

*In this study, the true strain is calculated by $\epsilon = \ln(1 + \epsilon_c)$, where $\epsilon_c = \Delta L/L_o$ is the conventional strain, in which ΔL and L_1 are the axial elongation and the initial gauge length of specimens. The true stress is calculated by $\sigma = P(1 + \epsilon_c)/A_o$, where P is the total axial tensile force and A_o is the initial cross-sectional area of the specimens.

various strain rates at -5℃. It is seen that strain rate has a strong effect on the stress-strain behavior of the frozen silt. The brittle behavior of the frozen soil increases with increasing strain rate. At strain rates greater than about 10^{-2}/s, the soil exhibits a brittle type fracture, which is characterized by a smaller failure strain (less than 0.5%) and a nearly straight σ-ϵ curve. For this type of failure, the elasticity of the material essentially governs its mechanical behavior. For $\dot{\epsilon} < 10^{-2}$/s the sample exhibits a ductile or a moderately brittle type failure, characterized by a significant plastic flow following a small elastic deformation.

It should be noted that for relatively low strain rates (say, $< 10^{-5}$/s), the σ-ϵ curves rapidly drop down from their peak at a small strain of less than 0.5%. This type of σ-ϵ behavior is completely different from that observed in compression, where

Table 1. Tension test results of frozen Fairbanks silt at -5°C.

Specimen no.	Machine speed v (cm/min)	Peak strength σ_m (kg/cm²)	Failure strain ϵ_f (%)	Time to failure t_m (s)	Average strain rate $\dot{\epsilon}$ (/s)	Initial tangent modulus E_i ($\times 10^4$) (kg/cm²)	50% peak strength modulus E_i ($\times 10^4$) (kg/cm²)
			Medium density				
12-4	5.9×10^{2}	58.9	0.240	7.00×10^{-1}	3.43×10^{-1}	—	—
12-3	5.9×10^{1}	58.2	0.390	8.00×10^{-2}	4.88×10^{-2}	—	—
11-4	5.9×10^{1}	72.5	—	8.00×10^{-2}	4.88×10^{-2}	—	—
12-2	5.9×10^{1}	63.6	—	8.00×10^{-2}	4.88×10^{-2}	—	—
11-3	5.9×10^{1}	73.4	—	8.00×10^{-2}	4.88×10^{-2}	—	—
12-1	5.9×10^{0}	65.5	0.770	7.80×10^{-1}	9.87×10^{-3}	—	—
5-2	5.9×10^{0}	81.1	0.650	7.00×10^{-1}	9.30×10^{-3}	—	—
6-1	5.9×10^{0}	75.2	0.800	1.00×10^{0}	8.00×10^{-3}	—	—
4-2	5.9×10^{-1}	44.4	1.215	1.20×10^{1}	1.01×10^{-3}	—	—
4-3	5.9×10^{-1}	48.7	1.500	1.50×10^{1}	1.00×10^{-3}	—	—
17-2	5.9×10^{-1}	47.1	1.824	1.90×10^{1}	9.60×10^{-4}	—	—
17-4	5.9×10^{-1}	51.6	1.482	1.40×10^{1}	1.06×10^{-3}	—	—
3-4	5.9×10^{-2}	31.6	1.049	1.10×10^{2}	1.00×10^{-4}	10.0	—
4-1	5.9×10^{-2}	32.0	1.128	1.10×10^{2}	1.03×10^{-4}	11.0	1.35
4-4	5.9×10^{-3}	22.4	1.224	1.24×10^{3}	1.07×10^{-5}	5.0	0.93
5-3	5.9×10^{-3}	21.0	0.574	7.24×10^{2}	7.93×10^{-4}	13.0	1.00
5-4	5.9×10^{-3}	22.6	0.936	9.04×10^{2}	1.04×10^{-5}	12.0	1.30
6-2	5.9×10^{-4}	18.0	0.402	4.86×10^{3}	8.27×10^{-7}	14.8	1.80
6-3	5.9×10^{-4}	19.2	0.477	6.30×10^{3}	7.57×10^{-7}	11.0	2.00
11-1	5.9×10^{-5}	16.7	0.334	4.44×10^{4}	7.52×10^{-8}	9.5	1.58
11-2	5.9×10^{-5}	14.8	0.295	4.68×10^{4}	6.30×10^{-8}	9.0	1.30
			High density				
15-1	5.9×10^{-1}	44.3	2.608	2.40×10^{1}	1.09×10^{-3}	—	—
15-2	5.9×10^{-1}	43.7	2.585	2.40×10^{1}	1.08×10^{-3}	—	—
9-2	5.9×10^{-2}	27.8	1.665	1.52×10^{2}	1.10×10^{-4}	12.0	0.80
9-1	5.9×10^{-2}	29.8	1.946	1.40×10^{2}	1.39×10^{-4}	12.0	0.89
15-3	5.9×10^{-3}	20.3	1.282	1.46×10^{3}	8.78×10^{-6}	12.0	1.00
9-3	5.9×10^{-3}	25.3	1.660	1.38×10^{3}	1.20×10^{-5}	9.5	1.10
9-4	5.9×10^{-4}	16.4	0.387	5.64×10^{3}	6.86×10^{-7}	9.0	1.30
15-4	5.9×10^{-4}	15.3	0.698	7.32×10^{3}	9.54×10^{-7}	6.8	0.81
			Low density				
18-2	5.9×10^{0}	41.2	0.250	4.00×10^{-1}	6.25×10^{-3}	—	—
18-3	5.9×10^{0}	45.7	—	8.00×10^{-1}	6.25×10^{-3}	—	—
18-1	5.9×10^{-1}	51.9	0.480	1.00×10^{1}	4.80×10^{-4}	—	—
16-1	5.9×10^{-1}	46.5	0.389	7.00×10^{0}	5.56×10^{-4}	—	—
10-1	5.9×10^{-2}	39.9	0.998	2.02×10^{2}	4.95×10^{-5}	13.7	1.54
10-2	5.9×10^{-2}	37.1	0.874	1.88×10^{2}	4.65×10^{-5}	11.0	1.50
10-3	5.9×10^{-3}	26.7	0.586	1.35×10^{3}	4.33×10^{-6}	19.0	1.40
16-2	5.9×10^{-3}	25.4	0.632	1.02×10^{3}	6.22×10^{-6}	18.3	1.36
10-4	5.9×10^{-4}	20.4	0.548	1.06×10^{4}	5.19×10^{-7}	16.8	1.60
16-3	5.9×10^{-4}	17.5	0.449	8.00×10^{3}	5.61×10^{-7}	13.0	1.40

Table 2. Tension test results of frozen medium-density Fairbanks silt at -2°C.

Specimen no.	Machine speed v (cm/min)	Peak strength σ_m (kg/cm²)	Failure strain ϵ_f (%)	Time to failure t_m (s)	Average strain rate $\dot{\epsilon}$ (/s)	Initial tangent modulus E_i ($\times 10^4$) (kg/cm²)	50% peak strength modulus E_i ($\times 10^4$) (kg/cm²)
19-3	5.9×10^{1}	40.7	—	—	9.00×10^{-2}	—	—
19-4	5.9×10^{1}	38.8	—	—	9.00×10^{-2}	—	—
19-1	5.9×10^{0}	48.4	0.540	6.00×10^{-1}	9.00×10^{-3}	—	—
19-2	5.9×10^{0}	52.4	—	—	9.00×10^{-3}	—	—
13-2	5.9×10^{-1}	30.4	1.987	2.00×10^{1}	1.00×10^{-3}	—	—
13-3	5.9×10^{-1}	26.1	1.751	1.60×10^{1}	1.60×10^{-3}	—	—
13-4	5.9×10^{-1}	26.6	1.550	1.60×10^{1}	9.69×10^{-4}	—	—
8-3	5.9×10^{-2}	20.9	1.465	1.85×10^{2}	7.92×10^{-5}	6.0	0.84
8-4	5.9×10^{-2}	23.6	1.301	1.32×10^{2}	9.86×10^{-5}	7.0	0.80
2-1	5.9×10^{-2}	19.0	1.290	1.68×10^{2}	7.69×10^{-5}	6.5	—
1-3	5.9×10^{-2}	14.6	0.858	3.60×10^{2}	2.38×10^{-5}	6.9	0.70
14-3	5.9×10^{-4}	7.8	0.900	8.64×10^{3}	1.04×10^{-6}	4.6	0.35
14-4	5.9×10^{-4}	7.7	0.881	8.64×10^{3}	1.02×10^{-6}	5.0	0.30

Table 3. Tension test results of frozen medium-density Fairbanks silt at a machine speed of 0.059 cm/min.

Specimen no.	Temperature θ (°C)	Peak strength σ_m (kg/cm²)	Failure strain ϵ_f (%)	Time to failure t_m (s)	Average strain rate $\dot{\epsilon}$ (/s)	Initial tangent modulus E_i ($\times 10^4$) (kg/cm²)	50% peak strength modulus E_i ($\times 10^4$) (kg/cm²)
14-1	- 1.0	16.8	2.194	2.20×10^{2}	9.97×10^{-5}	6.0	0.55
14-2	- 1.0	16.1	2.665	2.72×10^{2}	9.80×10^{-5}	5.6	0.50
8-3	- 2.0	20.9	1.465	1.85×10^{2}	7.92×10^{-5}	6.0	0.84
8-4	- 2.0	23.6	1.301	1.32×10^{2}	9.86×10^{-5}	7.0	0.80
2-1	- 2.0	19.0	1.290	1.68×10^{2}	7.69×10^{-5}	6.5	0.80
8-1	- 3.0	25.2	1.153	1.20×10^{2}	1.20×10^{-4}	8.5	1.00
8-2	- 3.0	25.2	1.533	1.48×10^{2}	1.04×10^{-4}	8.5	1.00
3-4	- 5.0	31.6	1.049	1.10×10^{2}	1.00×10^{-4}	10.0	—
4-1	- 5.0	32.0	1.128	1.10×10^{2}	1.03×10^{-4}	11.0	1.35
7-3	- 7.0	41.1	1.257	1.50×10^{2}	8.38×10^{-5}	12.8	1.80
7-4	- 7.0	41.5	1.028	1.40×10^{2}	7.34×10^{-5}	14.0	1.80
6-4	-10.0	58.6	0.837	1.30×10^{2}	6.44×10^{-5}	16.0	2.40
7-1	-10.0	50.9	1.468	1.86×10^{2}	7.90×10^{-5}	17.6	2.35
7-2	-10.0	56.8	1.209	1.52×10^{2}	7.95×10^{-5}	16.8	2.20

the materials sustain a significant stress level after initial yielding. Because of this, great care must be taken in engineering design where the long-term tensile strength of frozen soils needs to be considered.

Figure 11 shows a set of σ–ϵ curves of the medium-density samples for various temperatures at a strain rate of 10^{-4}/s. Obviously, the brittleness of the sample increases with decreasing temperature. However, the failure mode is less dependent on temperature than on strain rate. All of the σ–ϵ curves for temperatures varying from -1 to -7°C (Fig. 11) reflect a similar level of plasticity. Even at a lower temperature of -10°C, no brittle fracture was observed.

Figure 12 presents some typical σ–ϵ curves of the specimens with different dry densities at a strain rate of about 10^{-4}/s and a temperature of -5°C. The σ–ϵ curve appears to be somewhat sharper for the specimen with lower density than for higher density, indicating a slight loss of ductility with decreasing density.

Two specimens after testing are shown in Figure 13. It seems that as brittleness increases, the fracture plane of the specimens becomes flatter.

Peak tensile strength, σ_m

Strain rate dependence of the peak strength

The peak tensile strength σ_m of the frozen silt with medium density as a function of $\dot{\epsilon}$ at -2 and -5°C is plotted in Figure 14. The ductile–brittle (*D–B*) transition occurs at almost the same strain rate of about 10^{-2}/s at both -2 and -5°C, indicating that the critical strain rate of the *D–B* transition is not sensitive to temperature in this temperature range for the medium-density Fairbanks silt. It was found, however, that this critical strain rate varies with dry density.

Figure 15 presents a log–log plot of σ_m vs $\dot{\epsilon}$ for various dry densities at -5°C. It shows that, for lower density, the critical strain rate decreases to about 5×10^{-4}/s. Based on this observation, one may infer that the critical rate of *D–B* transition for ice should be lower than the above value. According to Mellor (1972), this is true. He reported that the ductile–brittle transition occurs at a strain rate of about 10^{-4}/s for polycrystalline ice at -7°C. Unfortunately, we did not run the high strain rate tests on the high-density samples, so the *D–B* transition rate for high density could not be determined in this study. According to Haynes (1975), it is about 10^{-2}/s at -9.4°C.

Note that Figure 14 shows another break point at a strain rate of 10^{-5}/s on the $\log\dot{\epsilon}$ – $\log\sigma_m$ curve for -5°C. Reviewing Figure 10, one can see that a significant drop in failure strain (from about 1% to 0.4%) also occurs at this strain rate. This evidence may indicate a change in deformational mechanisms at this critical strain rate.

From Figures 14 and 15, the peak strength σ_m as a function of strain rate can be described by a simple power-law equation within the range of strain rate applied:

$$\sigma_m = k(\dot{\epsilon}/\dot{\epsilon}_1)^n \qquad (3)$$

where $\dot{\epsilon}_1$ is a reference strain rate taken as 1.0/s, n is a dimensionless parameter, and k has the dimension of stress. Both k and n vary with temperature, density, and the range of strain rates. The values of k and n determined from the test data by linear regression analysis are shown in Table 4.

It is interesting to compare the strain rate dependence of tensile strength with that of compressive strength. The comparison for -5°C is shown in Figure 16, in which the compression data are from the authors' recent report (Zhu and Carbee 1984). It is seen from this figure that for $\dot{\epsilon}$ less than 10^{-2}/s, the peak tensile strength is close to the peak compressive strength. However, for $\dot{\epsilon}$ greater than 10^{-2}/s, the former is much less than the latter. Haynes (1975) observed a similar bifurcation at a strain rate of about 10^{-2}/s for Fairbanks silt with high density at -9.4°C. Hawkes and Mellor (1972) reported a bifurcation of the two strengths at about 10^{-6}/s for polycrystalline ice. Further micromechanistic studies are needed to discover the physical reasons for this bifurcation.

Table 4. Values of k and n in equation 3.

θ (°C)	γ_d (g/cm³)	$\dot{\epsilon}$ (/s)	k (kg/cm²)	n
-5	1.08–1.12	5×10^{-4} – 5×10^{-7}	148.6	0.142
	1.20–1.26	1×10^{-2} – 1×10^{-5}	143.4	0.151
		1×10^{-5} – 6×10^{-8}	48.6	0.068
	1.36–1.41	1×10^{-3} – 7×10^{-7}	105.4	0.134
-2	1.20–1.26	1×10^{-2} – 1×10^{-6}	103.2	0.185

Time dependence of the peak strength

The peak tensile strength σ_m as a function of time to failure t_m for various dry densities and temperatures is shown in Figures 17 and 18, respectively. It is obvious that the peak strength as a function of time to failure t_m has an upper limit, i.e., the limiting instantaneous strength σ_0.

In a ductile failure regime, σ_m rapidly decreases with increasing t_m until t_m reaches about 200 s, and then σ_m decreases very slowly with increasing t_m. In a brittle fracture regime, σ_m decreases slightly with decreasing t_m. The average values of σ_0 obtained from the present study are shown in Table 5. The time to failure corresponding to σ_0 is relatively insensitive to temperature for the range tested, but varies with density. It has a value of about 1 second for the silt with medium density and about 10 seconds for low density.

Replotting Figure 18 in the coordinates of $1/\sigma_m$ vs $\log t_m$, as shown in Figure 19, one can see that the tensile strength of the frozen silt as a function of time to failure for the ductile failure regime can

Table 5. Average values of σ_0 for frozen Fairbanks silt.

θ (°C)	σ_0 (kg/cm²) Medium density	σ_0 (kg/cm²) Low density
-2	50.4	—
-5	73.9	49.2

be well described by Vialov's (1959) strength equation:

$$\sigma_m = \frac{\beta}{\log(t_m/B)} \quad (4)$$

where β and B are empirical parameters. β has the dimension of stress, and B has the dimension of time. For a particular type of soil, both β and B depend upon temperature and density. The values of β and B obtained from the test data are shown in Table 6. Note that the strength-time data for brittle fracture could not be used to determine the values of β and B in eq 4.

Temperature dependence of the peak strength

Figure 20 presents a log-log plot of σ_m vs θ/θ_0 for the samples with medium density at an average strain rate of about 10^{-4}/s. It shows a break point at the temperature of -5°C, and the peak strength increases more rapidly with decreasing temperature when $\theta < -5$°C. From this figure, σ_m as a function of θ can be described by a power-law equation within a certain range of temperature:

$$\sigma_m = A(\theta/\theta_0)^m \quad (5)$$

where θ is the negative temperature in °C, θ_0 is a reference temperature taken as -1°C, and A and m are empirical parameters. From these test results, they depend upon temperature. The values of A and m, together with the correlation coefficient γ and data points N obtained from the test results, are shown in Table 7.

Figure 21 presents a log-log curve of unfrozen water content against temperature for the silt with a water content of 40.5%, which is plotted using the data shown in Appendix B. It is interesting to note that the log-log curve of w_u vs β/θ_0 also breaks at -5°C (Fig. 21).

Table 6. Values of β and B in equation 4.

θ (°C)	γ_d (g/cm³)	β (kg/cm²)	B (s)
	1.08–1.12	66.7	3.4
-5	1.20–1.26	80.1	0.3
	1.36–1.41	65.9	1.1
-2	1.20–1.26	21.4	14.6

Table 7. Values of A and m in equation 5 for $\dot{\epsilon} = 10^{-4}$/s and γ_d = 1.20–1.26 g/cm³.

θ (°C)	A (kg/cm²)	m	γ	N
-1 to -5	16.5	0.404	0.9892	8
-5 to -1	8.7	0.801	0.9855	7

Effect of density on the peak strength

The peak strength σ_m as a function of dry density γ_d for various machine speeds at -5°C is plotted in Figure 22. It is seen that for the saturated frozen silt, σ_m increases with decreasing γ_d in the ductile regime. Especially for relatively high strain rates and low density range, σ_m is more sensitive to γ_d. As is expected, this relationship can also be seen from a plot of σ_m vs i_v, as shown in Figure 23, in which the volume ice content i_v is calculated by eq 1. A similar relationship was observed between an initial compressive yield strength and dry density or between that and volume ice content (Sayles and Carbee 1981, Zhu and Carbee 1984), indicating that the tensile strength, like the initial yield strength in compression, is essentially governed by the fracturing of the ice matrix in frozen soil.

Failure tensile strain, ϵ_f

As defined before, the failure tensile strain ϵ_f refers to the strain at the peak tensile strength σ_m. Figure 24 shows failure strain ϵ_f as a function of $\dot{\epsilon}$ for the specimens with various densities at -5°C. Explicitly, ϵ_f increases with increasing $\dot{\epsilon}$ in the ductile failure regime, while it decreases with increasing $\dot{\epsilon}$ in the brittle regime. The maximum failure strain occurs at a strain rate of about 10^{-3}/s for medium density and 5×10^{-3}/s for low density, which is one order less than that corresponding to the limiting instantaneous strength σ_0.

Figure 24 also shows that for relatively high strain rates, failure strain increases considerably with increasing dry density. For example, at a strain rate of 10^{-3}/s, ϵ_f increases from about 0.4% to 2.6% as γ_d increases from 1.1 to 1.4 g/cm³ at -5°C. However, there is not a significant difference between the failure strains of the specimens with different densities at lower strain rates.

The failure strain as a function of temperature for a given machine speed and density is shown in Figure 25. It is clear that ϵ_f rapidly increases with increasing temperature for temperatures higher

than -2°C. This may be explained by the fact that as temperature rises above the significant phase transition temperature of about -2°C for the silt, the rapid increase in the unfrozen water content with temperature greatly increases the plasticity of the soil.

The failure strains from both the tension and compression tests on the medium-density specimens are compared in Figure 26. ϵ_f shows a similar variation with $\dot{\epsilon}$ for both tension and compression. However, the magnitude of ϵ_f in the tension tests is about one order less than in the compression tests.

Initial tangent modulus and 50% peak strength modulus

The initial tangent modulus E_i and modulus E_1 at 50% strength of the medium-density samples as a function of temperature are plotted on logarithm coordinates in Figures 27 and 28, respectively. The curves in the two figures break at -5°C; they can be described by a power-law equation within the range of temperature tested:

$$E_i, E_1 = a(\theta/\theta_0)^b \tag{6}$$

where parameters a and b depend upon the temperature range for a given soil. The values of a and b obtained from the test data are given in Table 8.

The initial tangent modulus and the 50% strength modulus as a function of $\dot{\epsilon}$ for various densities at -5°C are shown in Figures 29 and 30, respectively. It is seen that both E_i and E_1 are not dependent upon $\dot{\epsilon}$, but tend to increase with decreasing dry density.

Figure 31 presents a plot of E_i against E_1 for various test conditions. There seems to be a definite relationship between E_i and E_1, even though the data are scattered; it can be expressed as

$$E_i = 6.05E_1 + 3.26\times10^4 \tag{7}$$

where E_i and E_1 are in kg/cm². This relationship is helpful for determining E_i because E_1 is easier to determine from the test data.

For the sake of comparison, the E_i data of frozen Fairbanks silt reported by various researchers are cited as follows: Kaplar (1963) reported Young's modulus values from 2.25×10^5 to 2.39×10^5 kg/cm² within a range of temperature from 0 to -10°C by a dynamic method. Offensend (1966) found an average value of 2×10^5 kg/cm² from his tension tests at both -3.9 and -9.4°C; and Haynes (1975) reported an average value of about 7×10^4 kg/cm² from his tension tests on dense samples at -9.4°C.

Discussion of test techniques

End caps

The experiment shows that most of the samples tested under intermediate and slow speeds failed within gauge length. However, the specimen tested under fast speeds (say, $> 2\times10^{-2}$/s) frequently broke near the end cap, as shown in Figure 32. This is probably due to the stress concentrating in the specimen near the end caps during loading. Further studies need to be done to improve the end cap configuration.

Elongation measurement

Measuring the elongation of the neck section of a specimen in tension tests is a difficult problem. Considering the geometric configuration, Haynes (1975) presented a reduction procedure for calculating the strain in the neck section of a dumbbell specimen, based on the measured deformation between the two end caps. Following his procedure, we deduced

$$\Delta L = 0.665\Delta L_t \tag{8}$$

where ΔL_t is the observed deformation of the entire specimen between the two end caps and ΔL is the corrected deformation in the neck section.

In the present study, the deformation in the neck section of a specimen was directly measured by using two extensometers. As discussed earlier, for the sake of comparison, the deformation of the

Table 8. Values of a and b in equation 6.

	E_i				E_1			
θ (°C)	a ($\times10^4$) (kg/cm²)	b	γ	N	a ($\times10^4$) (kg/cm²)	b	γ	N
#1 to #5	5.50	0.381	0.9460	9	0.531	0.586	0.9946	8
#5 to #10	3.56	0.676	0.9758	7	0.402	0.762	0.9897	6

entire specimen between the two end caps was also measured for some of the tests, and eq 8 was used to compute the deformation in the neck section of the specimen. The observed and the calculated values of the strains at failure are compared in Figure 33. It shows that the strain up to failure calculated by using Haynes' reduction procedure is slightly (about 6%) less than the measured values.

Prevention of sublimation

The specimen data in Table B1 show that the saturation degree of the moist specimens coated with silicone, determined after the tests, is close to 100%. That is to say, coating a specimen with a thin layer of silicone does protect the specimen from sublimating for a certain period of elapsed time. To determine whether the silicone has an effect on the strength of the specimen, the following tests were carried out. Two replicate specimens were carefully prepared. One was enclosed in a plastic bag with the plastic mold inserts (used to form the necked portion of the specimen) still in place. The other was coated with silicone. After the two samples were tempered in an environmental chamber for 48 hours, they were tested at the same conditions. As shown in Figure 34, very similar σ–ϵ curves were observed for these two samples, indicating that the silicone layer has no significant effect on the results.

CONCLUSIONS

This investigation leads to the following conclusions.

1. The transition from ductile failure to brittle failure was observed occurring at a certain strain rate. This critical strain rate was found not to be sensitive to temperature for temperatures down to -5°C, but it varies with density. It is about 10^{-2}/s for medium-density and 5×10^{-4}/s for low-density silt at -5°C. For brittle fracture, the peak tensile strength slightly decreases with increasing strain rate, while for ductile failure, it significantly decreases with decreasing strain rate.

2. The peak tensile strength increases with decreasing temperature, and it increases more rapidly when the temperature is lower than -5°C.

3. The peak tensile strength increases with decreasing density, especially for lower densities.

4. The failure strain varies with strain rate and density, but does not depend upon temperature when temperature is lower than about -2°C.

5. Both the initial tangent modulus and the 50% strength modulus are found to be independent of strain rate, but significantly increase with the decrease in temperature and tend to decrease with the increase in density. The initial tangent modulus found in this study is about 17% of the Young's modulus determined by Kaplar (1963) at 1°C using a dynamic method and 83% at -10°C.

LITERATURE CITED

Hawkes, I. and M. Mellor (1972) Deformation and fracture of ice under uniaxial stress. *Journal of Glaciology,* **11**(61): 103–131.

Haynes, F.D., J.A. Karalius and J. Kalafut (1975) Strain rate effect on the strength of frozen silt. USA Cold Regions Research and Engineering Laboratory, Research Report 350. ADA-021 981.

Kaplar, C.W. (1963) Laboratory determination of the dynamic moduli of frozen soils and ice. In *Proceedings of 1st International Conference on Permafrost, Lafayette, Indiana, 11–15 Nov.* National Research Council, Building Research Advisory Board, pp. 293–301.

Offensend, F.S. (1966) The tensile strength of frozen soils. USA Cold Regions Research and Engineering Laboratory, Technical Note (unpublished).

Sayles, F.H. and D.L. Carbee (1981) Strength of frozen silt as a function of ice content and dry unit weight. *Engineering Geology,* **18**(1981): 55–56.

Vialov, S.S. (1959) Rheological properties and bearing capacity of frozen soils (Reologicheskie svoistva i nesushchaia sposobnost' merzlykh gruntov). Moscow, Izdvo AN SSSR. (Also USA Snow, Ice and Permafrost Research Establishment, Translation 74. AD-481 856.)

Zhu Yuanlin and D.L. Carbee (1984) Uniaxial compressive strength of frozen silt under constant deformation rates. *Cold Regions Science and Technology,* **9**(1984): 3–15.

Zhu Yuanlin and D.L. Carbee (In prep.) Creep and strength behavior of frozen silt in uniaxial compression. USA Cold Regions Research and Engineering Laboratory, CRREL Report.

Figure 1. Compacting specimens in the Lucite gang mold.

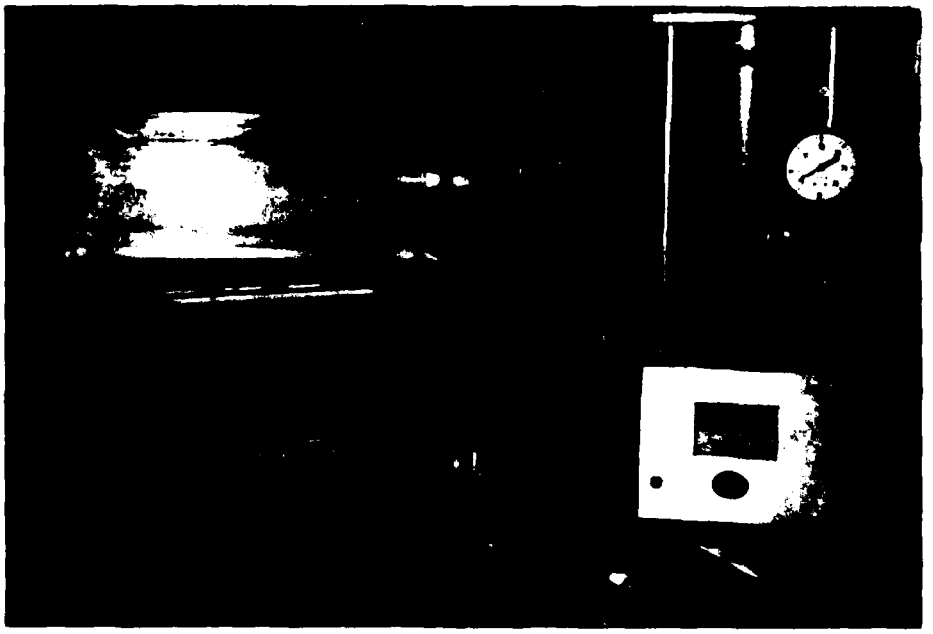

Figure 2. Saturation system set-up.

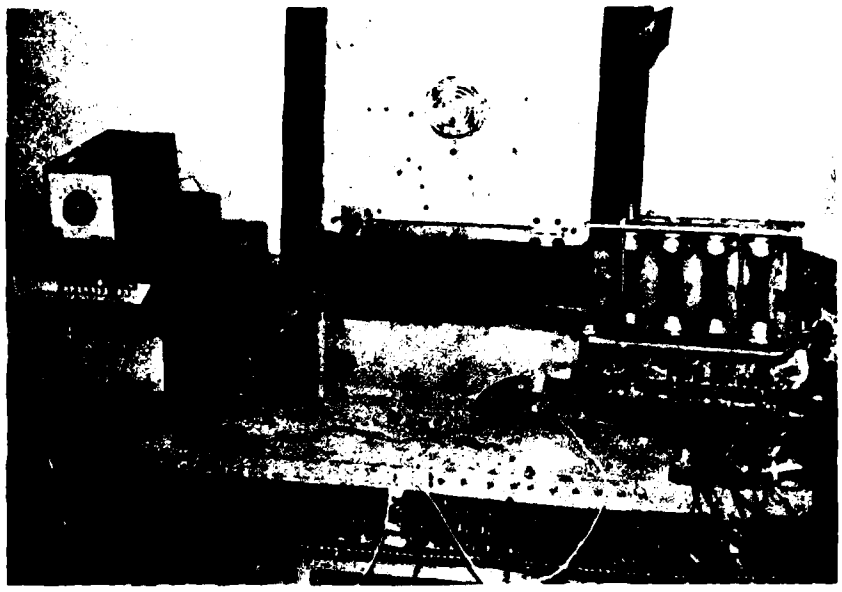

Figure 3. Freezing cabinet with a specimen-charged mold on the top.

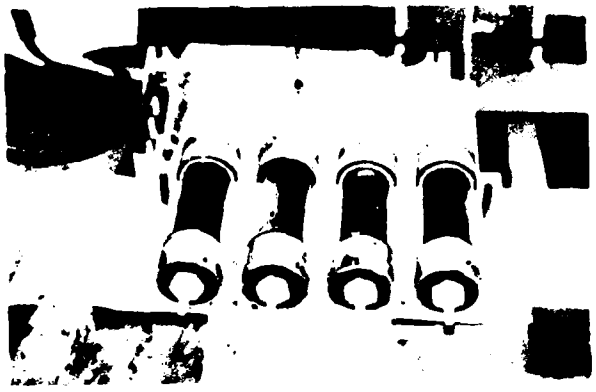

Figure 4. Disassembling the mold in a coldroom after freezing.

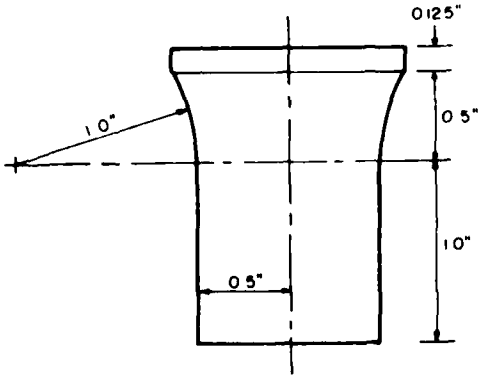

Figure 5. Geometry of one-half of the specimen.

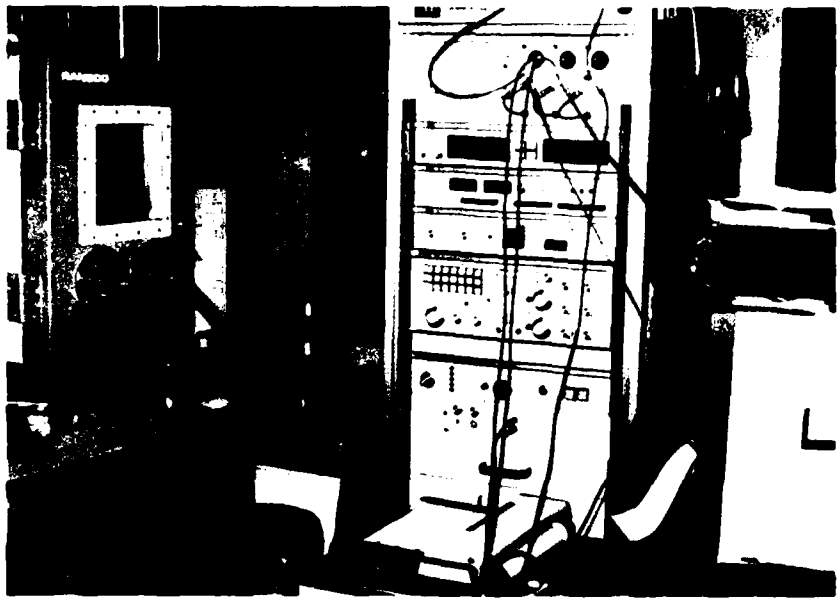

Figure 6. The Model 16000 MTS machine with a Ransco temperature-controlled cabinet.

Figure 7. A specimen bonded with two extensometers ready for testing.

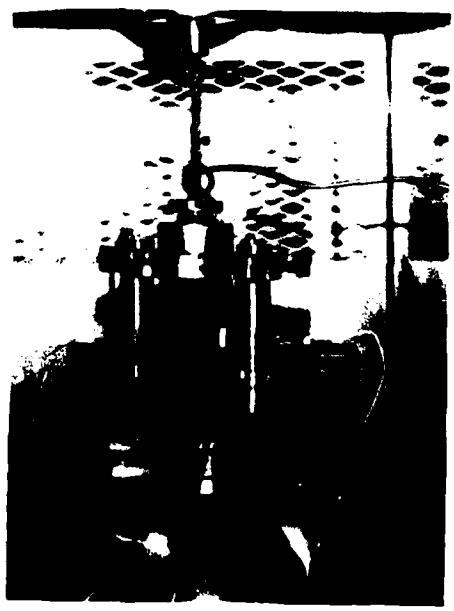

Figure 8. A specimen mounted with two extensometers and two LVDTs after testing.

Figure 9. The Model 1015 Biomation transient recorder and a Type 203 oscilloscope.

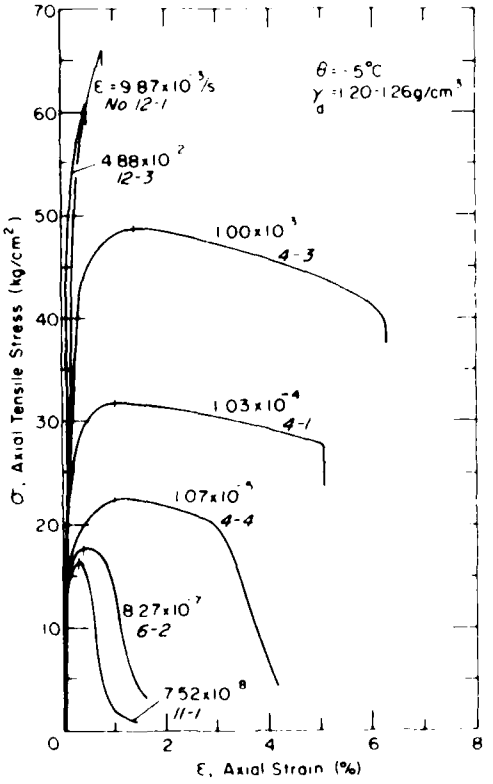

Figure 10. Typical set of stress-strain curves for various strain rates at -5°C.

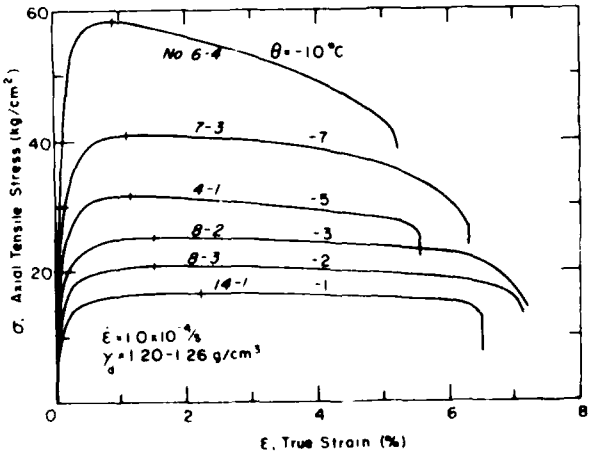

Figure 11. Typical set of stress-strain curves for various densities at a strain rate of 10^{-4}/s and a temperature of -5°C.

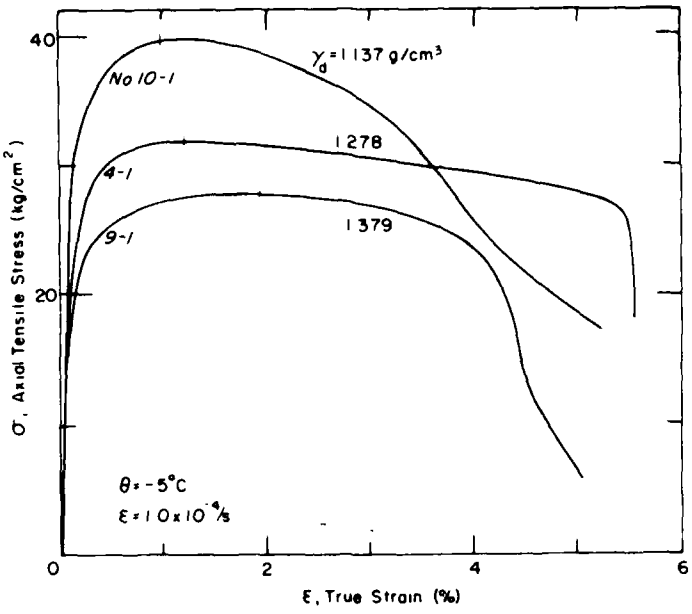

Figure 12. Stress-strain curves for various densities at a strain rate of 10^{-4}/s and a temperature of -5 °C.

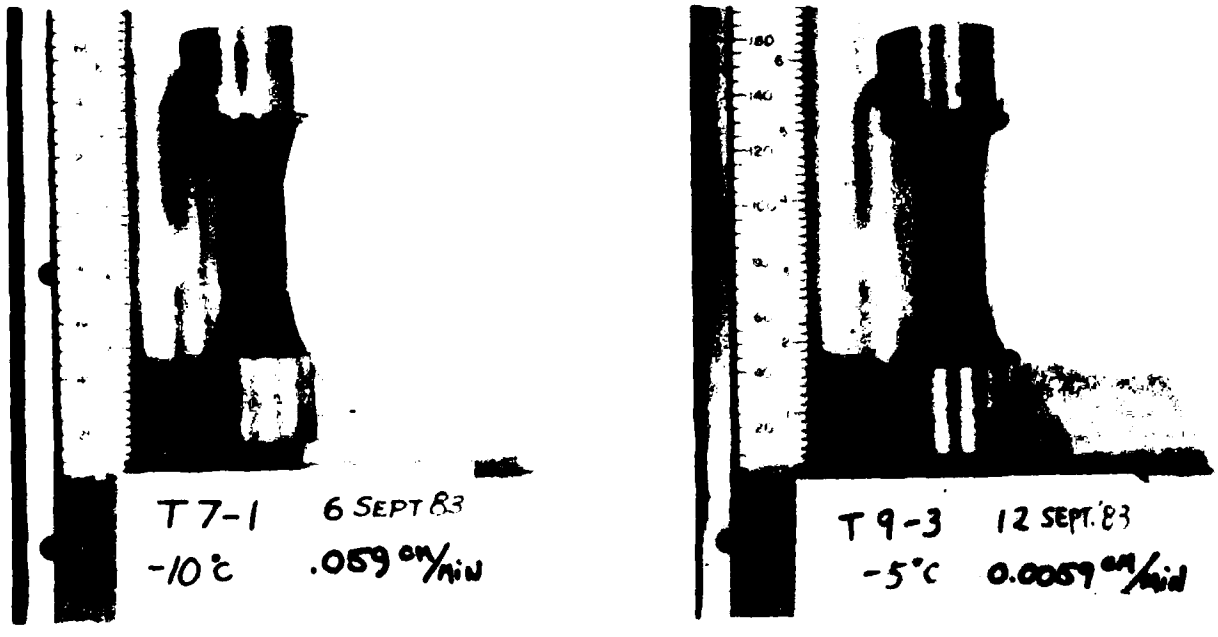

a. θ = −10°C, $\dot{\varepsilon}$ = 7.9×10⁻⁵/s, γ_d = 1.200 g/cm³.

b. θ = −5°C, $\dot{\varepsilon}$ = 1.2×10⁻⁴/s, γ_d = 1.355 g/cm³.

Figure 13. Typical Fairbanks silt specimens after tension tests.

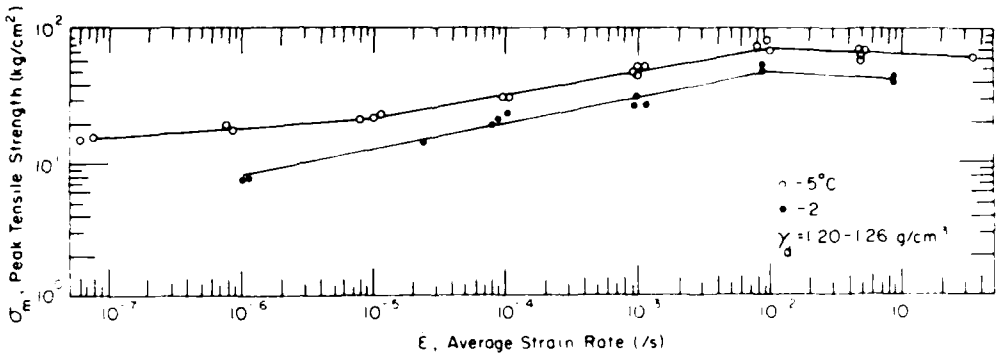

Figure 14. Peak strength of the specimens with medium density as a function of strain rate at -2 and -5°C.

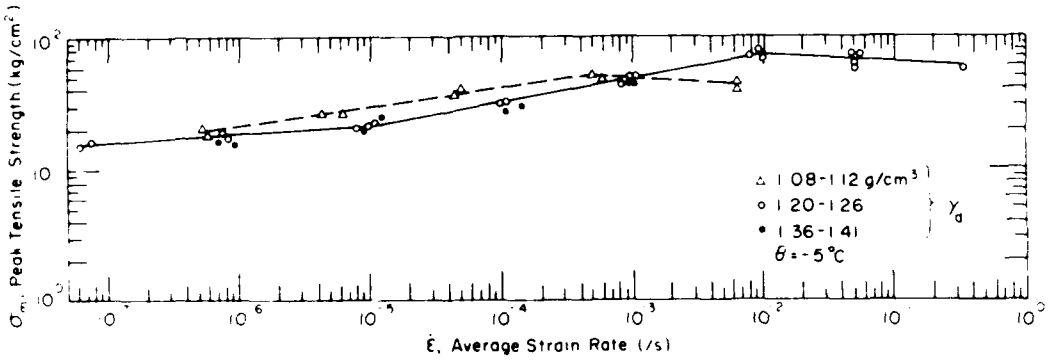

Figure 15. Peak strength as a function of strain rate for the specimens with various densities at -5°C.

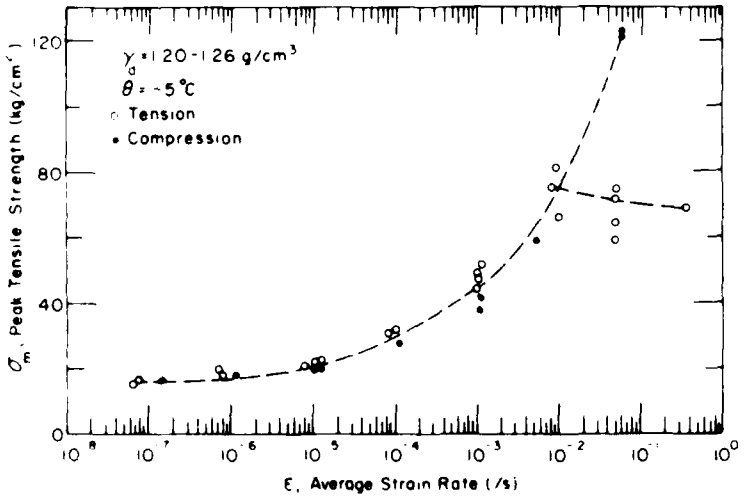

Figure 16. Peak tensile and compressive strength as a function of strain rate.

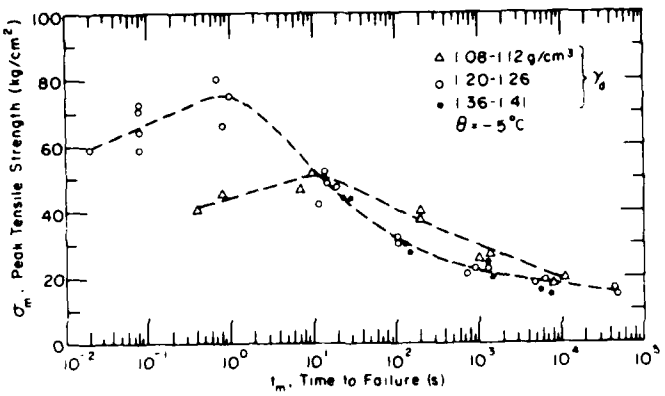

Figure 17. Peak tensile strength as a function of time to failure for the specimens with various densities at -5 °C.

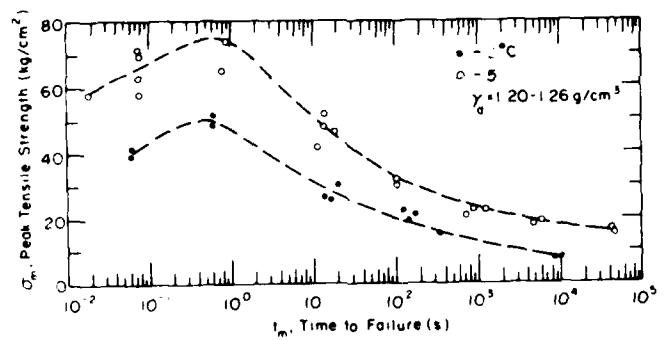

Figure 18. Peak tensile strength as a function of time to failure for the medium-density samples at -2 and -5 °C.

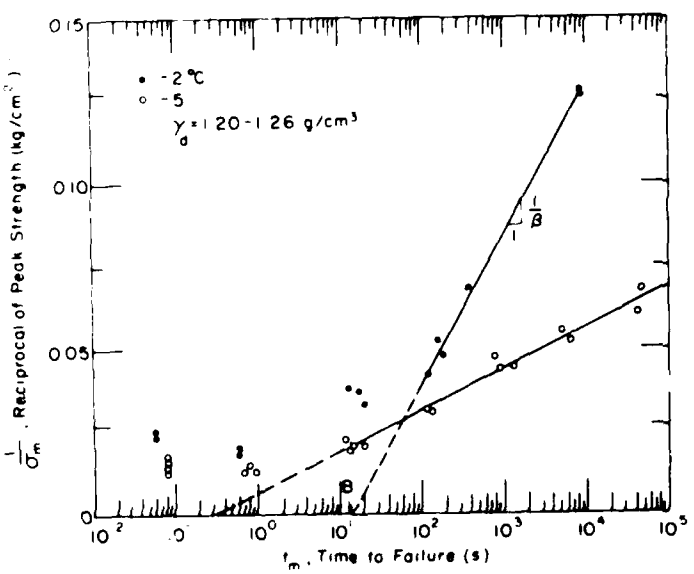

Figure 19. Plot of log 1/σ vs t_m for the medium-density samples at -2 and -5 °C.

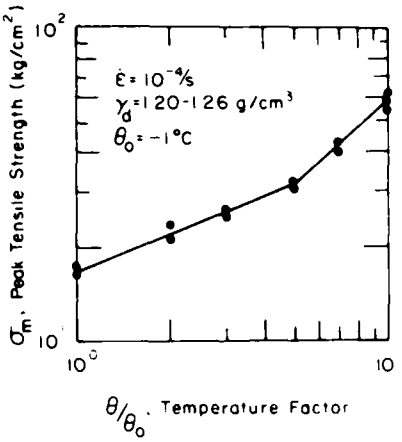

Figure 20. Log-log plot of peak tensile strength vs temperature for a strain rate of 10^{-4}/s.

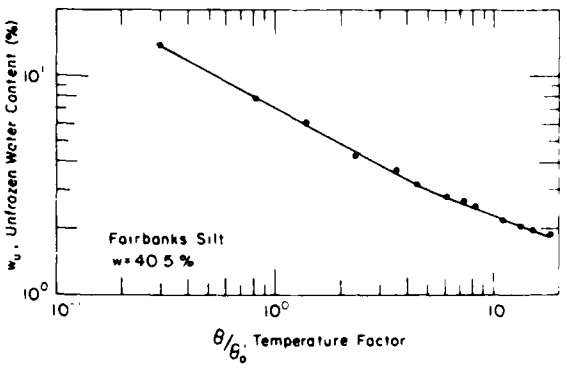

Figure 21. Unfrozen water content as a function of temperature for Fairbanks silt with a water content of 40.5%.

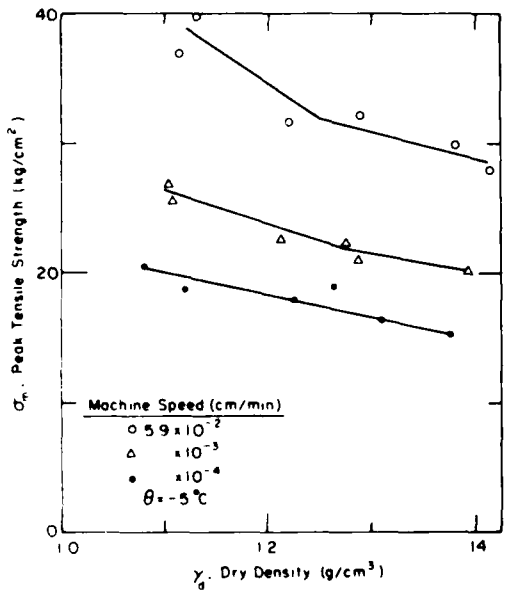

Figure 22. Peak tensile strength as a function of dry density for different machine speeds at -5°C.

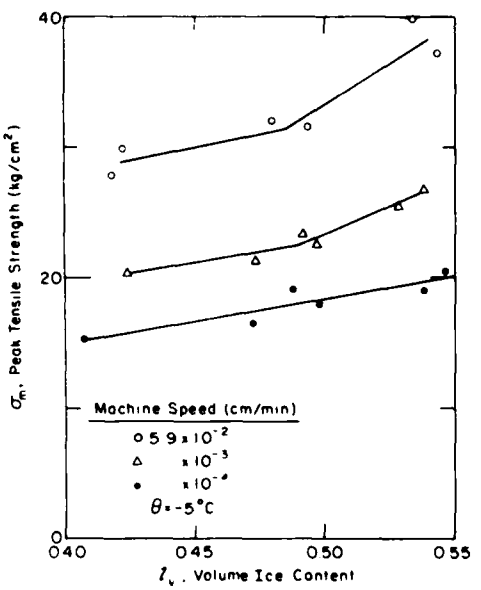

Figure 23. Peak strength as a function of volume ice content for different machine speeds at -5°C.

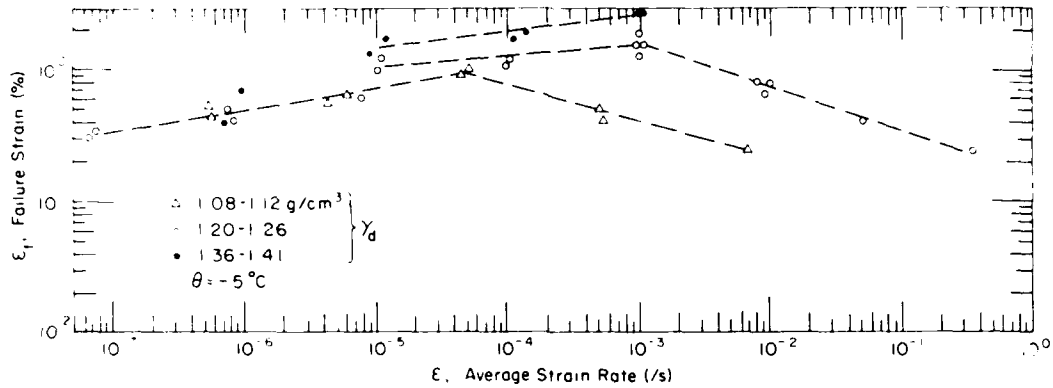

Figure 24. Failure strain as a function of average strain rate for various dry densities at -5 °C.

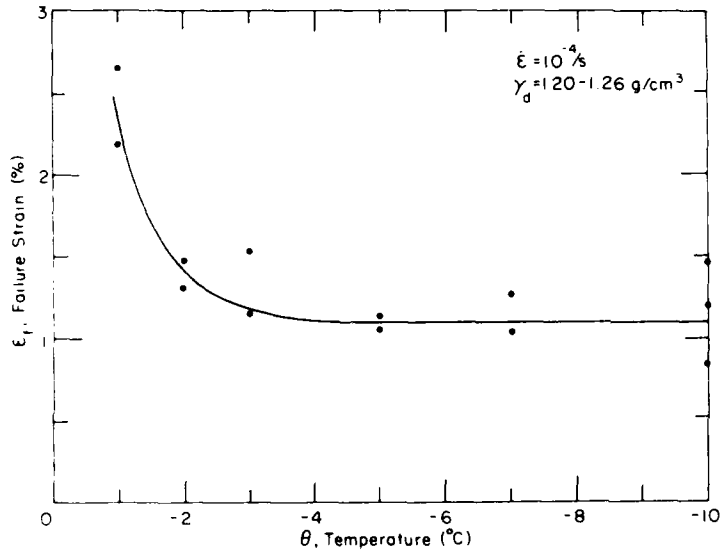

Figure 25. The variation of failure strain with temperature.

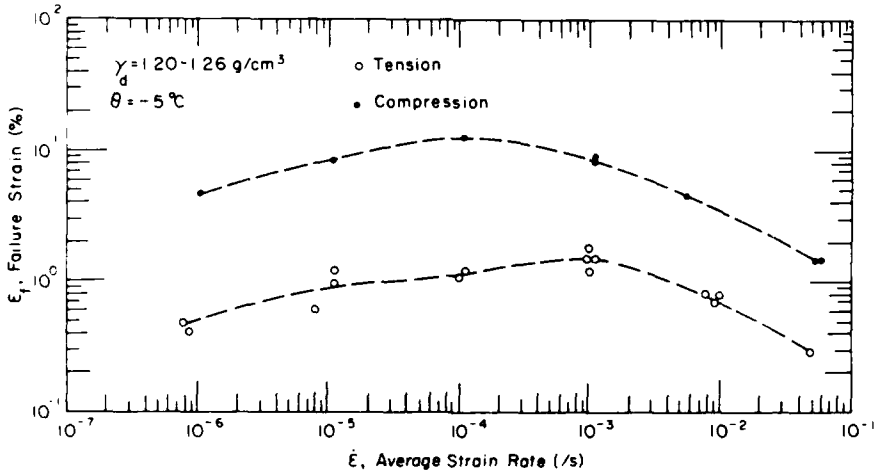

Figure 26. Comparison between the tensile failure strain and the compressive failure strain.

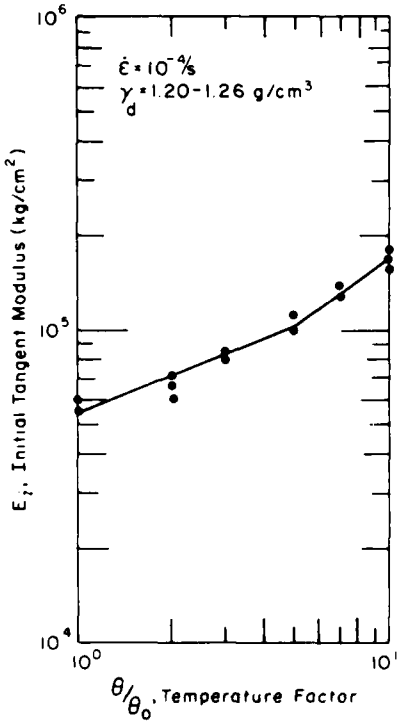

Figure 27. Log-log plot of E_i *vs* θ/θ_o.

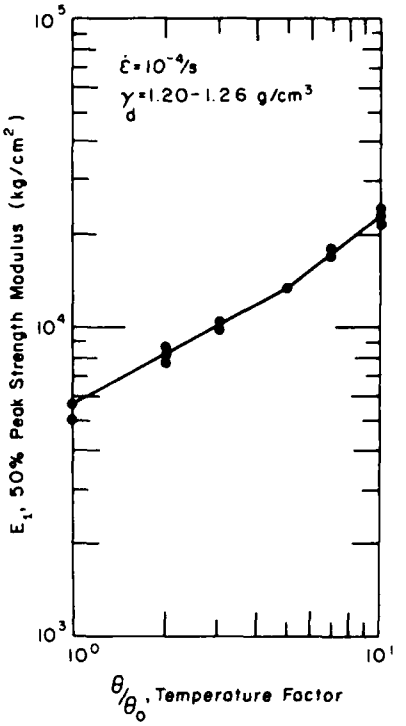

Figure 28. Log-log plot of E_i *vs* θ/θ_o.

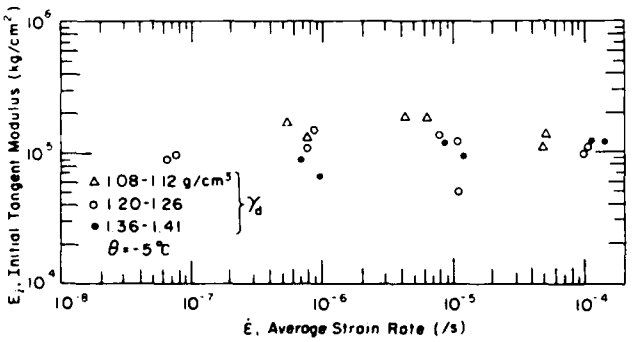

Figure 29. The variation of E_i *with strain rate for various dry densities at -5°C.*

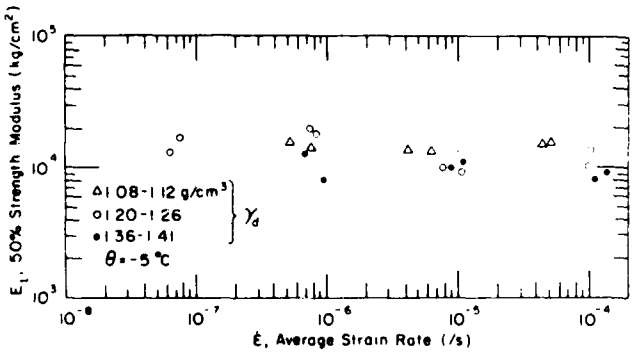

Figure 30. The variation of E_i *with strain rate for various dry densities at -5°C.*

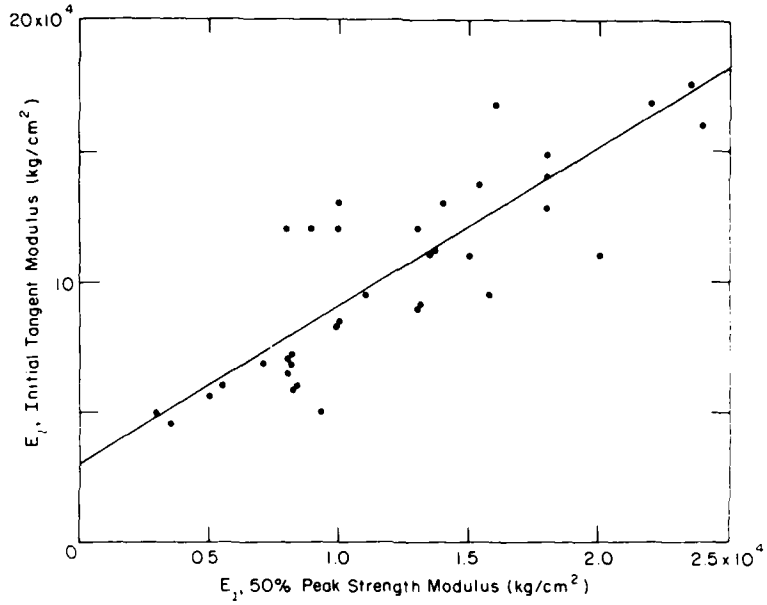

Figure 31. Relationship between E_i *and* E_1.

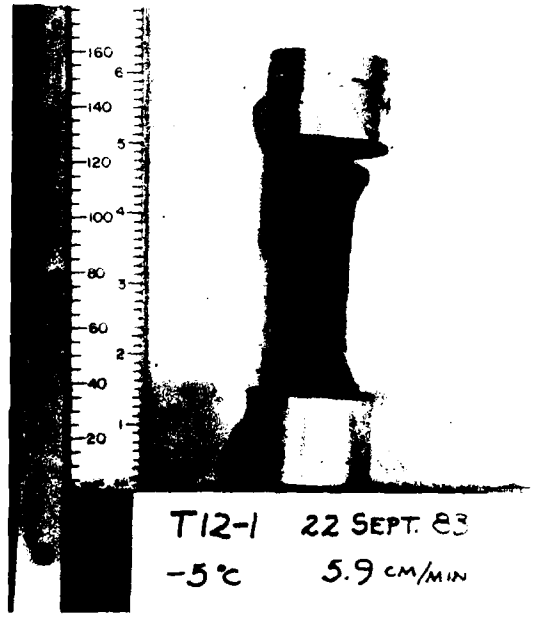

Figure 32. The specimen tested at a fast speed of 5.9 cm/min, showing a break near the end cap.

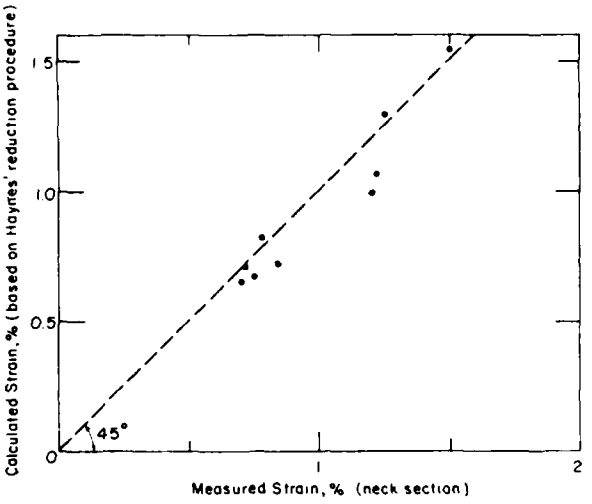

Figure 33. Comparison between the measured and the corrected strain in the neck section of specimens.

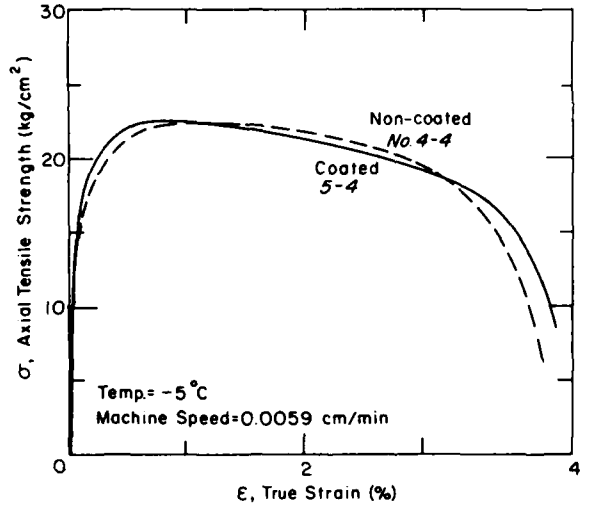

Figure 34. Comparison between the σ–ε curves of the coated and noncoated specimens.

APPENDIX A: PHYSICAL PROPERTIES OF FAIRBANKS SILT SPECIMENS

Specimen no.	Water content w (%)	Dry density γ_d (g/cm^3)	Volume ice content i_v	Saturation degree S (%)	Void ratio e	Porosity n
1-3	37.0	1.290	0.516	99.7	1.077	0.518
2-1	39.7	1.253	0.498	100.0	1.138	0.532
3-4	40.3	1.221	0.493	97.9	1.195	0.544
4-1	37.6	1.278	0.479	99.3	1.096	0.523
4-2	39.4	1.250	0.493	100.0	1.144	0.534
4-3	39.6	1.246	0.494	100.0	1.149	0.535
4-4	39.0	1.274	0.497	100.0	1.102	0.524
5-2	38.9	1.258	0.489	100.0	1.130	0.530
5-3	36.8	1.293	0.473	99.7	1.073	0.518
5-4*	40.3	1.214	0.491	97.0	1.207	0.547
6-1	39.2	1.266	0.496	100.0	1.117	0.528
6-2*	40.5	1.226	0.498	99.1	1.187	0.543
6-3*	38.8	1.259	0.488	100.0	1.126	0.530
6-4	43.6	1.171	0.554	98.4	1.289	0.563
7-1	41.8	1.200	0.516	98.7	1.233	0.552
7-2	40.9	1.213	0.538	98.6	1.209	0.547
7-3	40.6	1.218	0.503	98.4	1.200	0.545
7-4	42.1	1.203	0.516	99.9	1.227	0.551
8-1	41.3	1.206	0.489	98.4	1.220	0.550
8-2	42.3	1.185	0.493	97.7	1.260	0.558
8-3	43.6	1.173	0.494	98.7	1.284	0.562
8-4	42.8	1.193	0.492	100.0	1.244	0.554
9-1	31.3	1.379	0.422	96.6	0.942	0.485
9-2	30.3	1.415	0.418	98.6	0.893	0.472
9-3	33.2	1.355	0.443	98.8	0.976	0.494
9-4*	36.4	1.306	0.472	100.0	1.053	0.513
10-1	46.6	1.137	0.533	100.0	1.355	0.575
10-2	47.9	1.115	0.543	99.3	1.402	0.584
10-3	47.4	1.117	0.538	98.6	1.398	0.583
10-4*	49.6	1.080	0.546	97.3	1.482	0.597
11-1*	39.4	1.240	0.489	98.6	1.162	0.537
11-2*	39.6	1.238	0.491	98.8	1.163	0.538
11-3	39.9	1.251	0.500	100.0	1.142	0.533
11-4	39.9	1.238	0.495	99.4	1.165	0.538
12-1	40.1	1.243	0.500	100.0	1.156	0.536
12-2	40.1	1.243	0.500	100.0	1.156	0.536
12-3	39.3	1.254	0.493	100.0	1.135	0.532
12-4	41.0	1.245	0.513	100.0	1.152	0.535
13-2	39.1	1.247	0.464	98.4	1.149	0.535
13-3	40.0	1.229	0.469	98.0	1.181	0.541
13-4	37.5	1.263	0.448	96.6	1.122	0.529
14-1	38.6	1.248	0.431	96.9	1.147	0.534
14-2	38.0	1.275	0.432	99.3	1.102	0.524
14-3*	39.9	1.238	0.471	99.1	1.165	0.538

Specimen no.	Water content w (%)	Dry density γ_d (g/cm^3)	Volume ice content i_v	Saturation degree S (%)	Void ratio e	Porosity n
14-4	38.8	1.233	0.454	95.6	1.174	0.540
15-1	32.6	1.367	0.438	98.4	0.960	0.490
15-2	31.5	1.377	0.424	97.3	0.946	0.486
15-3	31.1	1.392	0.423	98.3	0.925	0.481
15-4*	30.4	1.373	0.407	92.5	0.952	0.488
16-1	48.7	1.108	0.549	99.7	1.419	0.587
16-2	46.8	1.112	0.528	96.4	1.410	0.585
16-3*	47.6	1.120	0.542	99.9	1.393	0.582
17-2	34.6	1.330	0.455	99.6	1.015	0.504
17-4	37.8	1.268	0.478	98.5	1.114	0.527
18-1	48.3	1.112	0.546	99.6	1.410	0.585
18-2	51.1	1.098	0.573	100.0	1.441	0.590
18-3	48.9	1.096	0.546	98.4	1.445	0.591
19-1	39.8	1.243	0.472	99.5	1.157	0.536
19-2	40.9	1.226	0.481	99.9	1.185	0.542
19-3	40.4	1.243	0.480	100.0	1.155	0.536
19-4	38.1	1.274	0.460	99.8	1.104	0.525

* Specimen coated with silicone.

APPENDIX B: UNFROZEN WATER CONTENT DATA OF FAIRBANKS SILT WITH THREE TYPICAL WATER CONTENTS

w = 30.3%*		w = 40.5%†		w = 49.9%†	
Temperature θ (°C)	Unfrozen water content w_u (%)	Temperature θ (°C)	Unfrozen water content w_u (%)	Temperature θ (°C)	Unfrozen water content w_u (%)
-15.55	3.06	-18.45	1.90	-18.50	2.17
-14.12	3.18	-15.44	1.98	-15.57	2.21
-10.85	3.13	-13.15	2.06	-13.39	2.23
- 8.95	3.48	-11.06	2.13	-11.09	2.26
- 6.86	3.55	- 8.40	2.53	- 8.48	2.71
- 4.96	4.13	- 7.36	2.72	- 7.44	2.80
- 3.86	4.43	- 6.15	2.80	- 6.09	3.03
- 2.62	4.90	- 4.43	3.19	- 4.51	3.56
- 1.76	5.55	- 3.62	3.65	- 3.52	3.86
- 1.48	6.42	- 2.36	4.31	- 2.44	4.45
- 1.06	7.83	- 1.40	6.25	- 1.1	5.57
- 0.88	7.95	- 0.82	6.78	- 0.82	6.90
- 0.54	8.12	- 0.30	13.77	- 0.28	13.85
- 0.51	8.53				
- 0.38	9.64				
- 0.33	11.86				
- 0.28	16.31				

* After Tice (unpublished)
† After Xu (unpublished)

A facsimile catalog card in Library of Congress MARC format is reproduced below.

Zhu Yuanlin

Tensile strength of frozen silt / by Zhu Yuanlin and David L. Carbee. Hanover, N.H.: U.S. Army Cold Regions Research and Engineering Laboratory; Springfield, Va.: available from National Technical Information Service, 1987.

v, 29 p., illus.; 28 cm. (CRREL Report 87-14.)

Bibliography: p. 8.

1. Frozen mechanics. 2. Frozen soil. 3. Silt. 4. Soil. 5. Strain. 6. Strength. I. Carbee, David L. II. United States. Army. Corps of Engineers. III. Cold Regions Research and Engineering Laboratory, Hanover, N.H. IV. Series: CRREL Report 87-14.

END

12-87

DTIC